HAL
open science

Towards the synthesis of mixed oxides with controlled stoichiometry from Prussian blue analogues

Virgile Trannoy, Amélie Bordage, Jordan Dezalay, Romuald Saint-Martin, Eric Rivière, Patricia Beaunier, Cédric Baumier, Camille La Fontaine, Giulia Fornasieri, Anne Bleuzen

To cite this version:

Virgile Trannoy, Amélie Bordage, Jordan Dezalay, Romuald Saint-Martin, Eric Rivière, et al.. Towards the synthesis of mixed oxides with controlled stoichiometry from Prussian blue analogues. CrystEngComm, 2019, 21 (23), pp.3634-3643. 10.1039/c9ce00427k . hal-02187860

HAL Id: hal-02187860

https://hal.science/hal-02187860v1

Submitted on 16 Aug 2021

HAL is a multi-disciplinary open access archive for the deposit and dissemination of scientific research documents, whether they are published or not. The documents may come from teaching and research institutions in France or abroad, or from public or private research centers.

L'archive ouverte pluridisciplinaire **HAL**, est destinée au dépôt et à la diffusion de documents scientifiques de niveau recherche, publiés ou non, émanant des établissements d'enseignement et de recherche français ou étrangers, des laboratoires publics ou privés.

Journal Name

ARTICLE TYPE

Cite this: DOI: 10.1039/xxxxxxxxxx

Towards the synthesis of mixed oxides with controlled stoichiometry from Prussian Blue analogues†

Virgile Trannoy,[a‡] Amélie Bordage,[*a] Jordan Dezalay,[a§] Romuald Saint Martin,[a] Eric Rivière,[a] Patricia Beaunier,[b] Cédric Baumier,[c] Camille La Fontaine,[d] Giulia Fornasieri,[a] and Anne Bleuzen[a]

Received Date
Accepted Date

DOI: 10.1039/xxxxxxxxxx

www.rsc.org/journalname

Controlling the synthesis of mixed oxides is of great interest since their stoichiometry influences the properties. We present here the transformation of the $Co_4[Fe(CN)_6]_{2.7}$ Prussian Blue Analogue (PBA) into the mixed $Co_{1.8}Fe_{1.2}O_4$ spinel oxide, with a detailed characterization of the final phase (obtained by calcination in air at 900°C during 2 hours) and an emphasis on the calcination process by TDA/TGA, X-ray diffraction, (High-resolution) TEM and Energy-filtered TEM. Single-crystalline particles with an homogeneous distribution of Fe and Co ions within each particle are observed, with the same Co:Fe ratio as in the PBA. The calcination mechanism is a 2-steps transformation, with first the elimination of water molecules and then the cyanide decomposition. XRD and TEM at intermediate temperatures additionally show the occurrence of a phase separation between 500°C and 850°C before the formation of the single final phase. We demonstrate also through the calcination of intermediate PBAs between $Co_4[Fe(CN)_6]_{2.7}$ and $Co_4[Co(CN)_6]_{2.7}$ that this synthesis route leads to the perfect control of the oxide stoichiometry through the control of the PBA. The versatility of this synthesis route is finally illustrated through the successful synthesis of $Co_{1.8}Fe_{1.2}O_4$ nanoparticles (diameter ∼5 nm) from PBA nanoparticles confined within the pores of a mesoporous silica monolith.

1 Introduction

Spinel ferrites are transition metal oxides of general formula $M_xFe_{2-x}O_4$, where M can be a transition metal, an alkali earth element or even a rare-earth element. The interest for these compounds significantly grew in the past decade thanks to the wide range of applications of these materials, e.g. in catalysis, depollution of water, energy storage (batteries, supercapacitors...), gas sensors, medicine applications, magnetic devices and data storage.[1–11] Such a wide range of applications arises from the priceless rich versatile chemistry of the spinel family, which offers the opportunity to adjust the stoichiometry to reach tailor-made properties. However, it is well-known that the properties of a spinel ferrite depends on its stoichiometry[5,12–15] and for a given targeted stoichiometry, also on the synthesis process.[1–3,16–24] Therefore many efforts have been devoted to the improvement of the synthesis process of the ferrite spinels in order to better control their stoichiometry and so their property.

One interesting way is the calcination in air of a precursor, whose stoichiometry, structure and synthesis are known and controlled. Prussian Blue Analogues (PBA) thus appear as a promising sacrificial compound, as their synthesis is well established and enables a full control of the PBA stoichiometry. They are coordination polymers with general formula $A_p[B(CN)_6]_q{\cdot}H_2O$ (A,B = transition metals) with a well-defined organization of the metallic cations at the atomic scale: the two transition metals are linked through a cyanide bridge, with an homogeneous repartition of the two transition metals at the atomic scale, thus leading to a face-centered cubic structure. Several studies already showed that when calcinated in air, PBAs (either bi- or trimetallic) are transformed into ternary or spinel oxides.[4,5,25–38]

In the particular case of Co ferrites, the $Fe_{1.8}Co_{1.2}O_4$ spinel oxide was obtained from the $Fe_3[Co(CN)_6]_2$ PBA for different

[a] ICMMO, Université Paris-Sud, Université Paris-Saclay, CNRS, 15 rue Georges Cl'emenceau, 91405 Orsay Cedex, France. Tel: +33 1 69 15 70 55; E-mail: amelie.bordage@u-psud.fr
[b] Sorbonne Université, CNRS, Laboratoire de Réactivité de Surface, LRS, F-75005 Paris, France.
[c] Centre de Sciences Nucléaires et de la Matière, Université Paris-Sud, CNRS/IN2P3, Université Paris-Saclay, 91405 Orsay Cedex, France.
[d] Synchrotron SOLEIL, Saint Aubin, 91190 Gif-sur-Yvette, France.

† Electronic Supplementary Information (ESI) available: [Evidence by Infra-Red spectroscopy of a thermally-induced charge transfer in **CoFe** below 300°C; Complete set of X-ray diffraction patterns between 300°C and 900°C].

‡ Present address: Institut des Matériaux Jean Rouxel, Université de Nantes, CNRS, 2 rue de la Houssinière, BP 32229, 44322 Nantes Cedex 3, France.
§ Present address: ISMO, Université Paris-Sud, Université Paris-Saclay, CNRS, 15 rue Georges Clémenceau, 91405 Orsay Cedex, France.

calcination conditions.[4,29] Nevertheless, these studies focused on the final product and its properties with no or few description of the PBA → spinel transformation process itself. Also, it is well-known that the Fe-rich ($CoFe_2O_4$) and the Co-rich ($FeCo_2O_4$) spinels do not present the same thermodynamic stability and that their synthesis is not possible over the same temperature range : using a low-temperature co-precipitation method, it was shown that $CoFe_2O_4$ was formed at 300°C, while $FeCo_2O_4$ could be formed as a single phase only around 900°C.[12,16] Therefore we undertook the detailed study of the formation of the $Co_{1.8}Fe_{1.2}O_4$ (called **CoFe-Ox** in the following) Co-rich counterpart of the $Fe_{1.8}Co_{1.2}O_4$ spinel[4,29] from the $Co_4[Fe(CN)_6]_{2.7}$ PBA (called **CoFe** in the following). In addition to the characterization of the final phase by X-Ray Diffraction (XRD) and both high-resolution and energy-filtered Transmission Electron Microscopy (TEM), we present a detailed study of the calcination process itself by thermodifferential/thermogravimetric analyses (TDA/TGA), XRD and TEM. From these results, we extend this thermal treatment optimized for a bimetallic PBA (i) to the formation of spinel ferrites of intermediate compositions between $Co_{1.8}Fe_{1.2}O_4$ and Co_3O_4, their stoichiometry being controlled by the precursor PBA one, and (ii) to the formation of single-cristalline 5nm-particles of the $Co_{1.8}Fe_{1.2}O_4$ spinel from the calcination of **CoFe** nanoparticles confined within the pores of a mesoporous silica monolith.

2 Experimental

2.1 Syntheses

The **CoFe** powdered $Co_4[Fe(CN)_6]_{2.7}$ PBA was prepared as already described elsewhere.[39] 400 mL of an aqueous solution of potassium hexacyanoferrate(III) (concentration of $2.5.10^{-3}$ mol.L^{-1}) were added dropwise during 3 hours and under stirring to 100 mL of an acidic aqueous solution of Co(II) nitrate (5.10^{-2} mol.L^{-1}, pH = 3). The resulting precipitate was centrifugated (15 minutes at 8000 rot.min^{-1}), washed three times with distilled water and centrifugated again. Finally it was allowed to dry in air at room temperature.

Intermediate chemical compositions between **CoFe** and the monometallic $Co_4[Co(CN)_6]_{2.7}$ PBA (called **CoCo**) were synthesized by a progressive replacement of Fe by Co in the starting $[Fe(CN)_6]^{3-}$ solution. The formula of the targeted PBA are $Co_4[(Co_{0.25}Fe_{0.75})(CN)_6]_{2.7}$ (called **Co(Co25)Fe**), $Co_4[(Co_{0.50}Fe_{0.50})(CN)_6]_{2.7}$ (called **Co(Co50)Fe**) and $Co_4[(Co_{0.75}Fe_{0.25})(CN)_6]_{2.7}$ (called **Co(Co75)Fe**).

To obtain the CoFe PBA/SiO_2 nanocomposite (called **NanoCoFe**), a Co^{2+}-containing mesoporous silica monolith[40] is impregnated with an acidic $[Fe(CN)_6]^{3-}$ solution using the double-solvent method.[41–43] This technique was already successfully applied to the synthesis of several PBAs as nanoparticles.[35,44–47] In previous studies, we also showed that all the Co cations initially present in the silica monolith are transformed in PBA[48] and that the PBA particles are entirely confined within the pores of the silica monolith.[40] The synthesis of the mesoporous silica monolith is described in Refs. 34, 39, 43 and 44.

2.2 Thermal treatment

After an optimization of the thermal treatment,[49] the transformation of **CoFe** into oxide (called **CoFe-Ox**) could be achieved by heating in air up to 900°C, with a heating rate of 5°C.min^{-1} followed by a 2-hours plateau at the targeted temperature. The same conditions of calcination were applied to the three Co-enriched PBAs (**Co(Co25)Fe**, **Co(Co50)Fe** and **Co(Co75)Fe**), leading to the three oxides **Co(Co25)Fe-Ox**, **Co(Co50)Fe-Ox** and **Co(Co75)Fe-Ox**.

To better understand the PBA-to-oxide transformation, a series of samples were also prepared from **CoFe** by heating at intermediate temperatures between room-temperature and 900°C (also with a 5°C.min^{-1} heating rate and a 2-hours plateau). The chosen temperatures are 300°C, 400°C, 500°C, 600°C, 700°C, 750°C, 800°C and 850°C; the corresponding oxides are called **CoFe-TTXXX**, where TT means Thermal Treatment and XXX is the corresponding temperature.

2.3 Materials characterizations

Elemental analyses were performed at the Service Central d'Analyses of the CNRS (Solaize, France).

Thermodifferential (TDA) and thermogravimetric (TGA) analyses were performed under air with a flow rate of 100 mL.min^{-1} and a temperature ramp of 5°C.min^{-1} up to 900°C using a TA Instruments SDT Q600 apparatus.

X-ray diffraction patterns were recorded using a Phillips PAN X'Pert PRO MPD X-ray diffractometer (Cu Kα_1; λ = 1.5418 Å). An aluminum sample holder was used for **CoFe** , the three intermediate compositions and the corresponding oxides. No background subtraction was performed on the XRD patterns. The lattice parameters were extracted using a simple Lebail fit for a $Fm3m$ space group in the case of the precursor PBA and a $Fd\bar{3}m$ space group in the case of the oxides.

Transmission Electron Microscopy (TEM) images were recorded using a JEOL JEM 100CXII electron microscope operating at an acceleration voltage of 100kV, whereas High-Resolution TEM (HR-TEM) images and EDX spectroscopy were performed using a JEOL JEM 2011 apparatus equipped with a LaB6 filament and operating at 200 kV; the images were collected using a 4008x2672 pixel CCD Camera (Gatan Orius SC1000) (LRS, Paris, France). EDX measurements were performed for different particles; the results are very close among the probed particles, so the given composition is representative of the whole sample. Additional images were taken using the FEI Tecnai G2 20 JANNuS-TEM (CSNSM/SCALP, Orsay, France) operating at an acceleration voltage of 200 kV with a spatial resolution of 0.23 nm; it is equipped with a GIF (Gatan Imaging Filter) Tridiem 863, which was used to acquire the energy-filtered images.

Magnetic measurements were recorded at room temperature with an MPMS-5S superconducting quantum interference device (SQUID) magnetometer for the four Co-Fe oxides (**CoFe-Ox**, **Co(Co25)Fe-Ox**, **Co(Co50)Fe-Ox** and **Co(Co75)Fe-Ox**). The samples were in powder form and placed in a capsule.

Fe and Co K-edges X-ray absorption spectroscopy was performed on **CoFe-Ox**, **Co(Co25)Fe-Ox**, **Co(Co50)Fe-Ox** and

This journal is © The Royal Society of Chemistry [year]

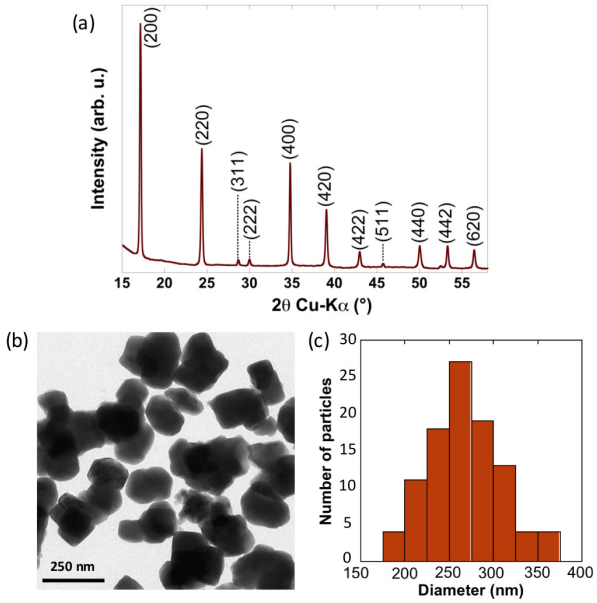

Fig. 1 (a) X-ray diffraction pattern, (b) TEM image and (c) size distribution of **CoFe**.

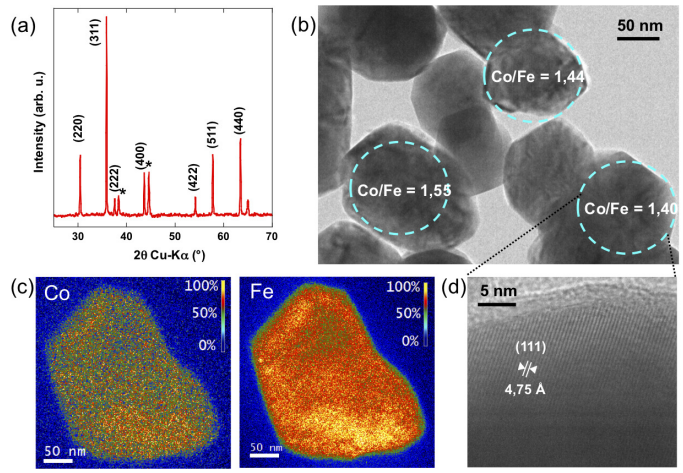

Fig. 2 Characterization of **CoFe-Ox** by (a) X-ray diffraction pattern, (b) TEM image (with Co:Fe ratio determined by EDX analyses indicated for some particles), (c) Co and Fe M_1-edge EFTEM images, and (d) HR-TEM image of a particle showing the (111) reticular planes. On the XRD pattern, the peaks marked with an asterisk arise from the aluminum sample holder.

Co(Co75)Fe-Ox. Co_3O_4 was also measured as a reference; we used the commercial product from Alfa Aesar. The spectra were recorded in the transmission mode on the ROCK beamline[50] at SOLEIL (Gif-sur-Yvette, France) using a Si(111) Quick-EXAFS monochromator. Spectra were recorded in a quick-scan mode from 6900 eV up to 8800 eV, allowing both edges to be recorded in a row to minimize experimental artefacts. Measurements were performed on pellets at room temperature. No radiation damage was observed.The spectra were energy-calibrated and normalized following the measurements.

3 Results and discussion

3.1 Characterization of CoFe

CoFe was characterized by XRD, TEM and elemental analyses. The exact chemical formula of **CoFe** is $K_{0.1}Co_4[Fe(CN)_6]_{2.7}\bullet 19H_2O$ (Table 1). The peaks of the diffraction pattern (Fig. 1a) can be indexed for the face-centered-cubic structure characteristic of PBA,[51,52] with a cell parameter of 10.31±0.02 Å. TEM images (Fig. 1b) show particles with a size distribution (Fig. 1c) ranging from 200 to 360 nm and centered around 250 nm.

Table 1 Elemental analysis results and proposed formula for **CoFe**.

	Fe	Co	C	N	H	K
Experimental (%)	12.27	19.38	16.89	19.56	3.10	0.33
Calculated (%)	13.10	20.48	16.89	19.70	3.28	0.34
Formula	$K_{0.1}Co_4[Fe(CN)_6]_{2.7} \bullet 19\ H_2O$					

3.2 Characterization of CoFe-Ox

CoFe-Ox (obtained after heating at 900°C during 2h) was characterized by XRD and TEM, and the main results are presented in Fig. 2.

The diffraction pattern of **CoFe-Ox** is presented Fig. 2a. Only sharp single peaks are observed, which indicates the presence of a single phase. They can be indexed by considering a spinel-type structure, with a cell parameter of 8.29±0.02 Å. This value is intermediate between the cell parameters of Co_3O_4 (a = 8.08±0.02 Å)[53] and $CoFe_2O_4$ (a = 8.38±0.01 Å),[12] and consistent with the cell parameter a = 8.24 Å of Co_2FeO_4.[12,16]

The size and shape of the particles were determined from TEM images (Fig. 2b). All particles are in the 100-350 nm size range. They also all have a Co:Fe ratio of 1.5±0.2 (Fig. 2b) as determined by EDX analyses; this is perfectly consistent with the Co:Fe initial ratio in **CoFe**, where Co:Fe = 4:2.7 = 1.48. Co and Fe M_1-edge Energy-filtered TEM (EFTEM) images also demonstrated that the Co and Fe ions are homogeneously distributed in the particle (Fig. 2c). High-resolution TEM enabled to give an image of the (111) reticular planes, which shows that the particles are single-cristalline. In addition, an inter-reticular distance (d_{111}) of 4.75 Å could be calculated from the HR-TEM image, which is consistent with the one from XRD (4.79 Å).

Given the spinel-type structure determined by XRD, **CoFe-Ox** has a $Co_xFe_yO_4$ formula, where $x+y = 3$. Therefore, as the Co:Fe ratio determined by EDX analyses is of 1.5, the proposed formula for **CoFe-Ox** is $Co_{1.8}Fe_{1.2}O_4$ (the absence of K traces was checked by TEM-EDX). This is fully consistent with previous results on the calcination of PBA into oxide, where the $Fe_{1.8}Co_{1.2}O_4$ oxide was obtained from the $Fe_3[Co(CN)_6]_2$ PBA.[4,29]

3.3 Monitoring of the PBA-to-oxide calcination by TDA/TGA

The thermodifferential and gravimetric analyses (TDA and TGA) of **CoFe** are presented in Fig. 3. Several temperature ranges can be identified.

First, up to ∼130°C (point A), a mass loss of 29% is observed, associated with a weak endothermic peak. It can be ascribed to the elimination of water molecules (both zeolitic and structural

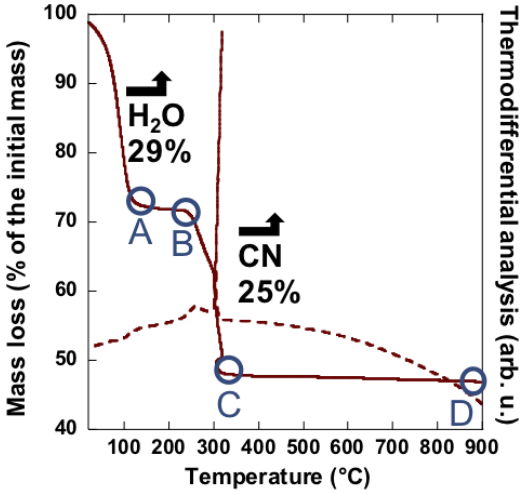

Fig. 3 TDA/TGA pattern recorded for **CoFe** with a heating rate of 5°C.min^{-1} in air. The continuous line is the mass and the dashed line the thermodifferential analysis.

ones), since this mass difference correponds to the total mass of the 19 water molecules initially present in **CoFe**.

A plateau in the mass loss is then observed between 130°C and 230°C (from point A to B in Fig. 3). Over this temperature range, the chemical formula of the compound can be given as $K_{0.1}Co_4[Fe(CN)_6]_{2.7}$. The first coordination shell of the Fe ions remains unchanged but, as already observed in the calcination of **CoCo**,[54] the average coordination number of the Co cations is now 4 since the two water molecules, which were part of their first coordination shell, are now eliminated.

Between 230°C and 315°C (from point B to C in Fig. 3), two successive mass losses are observed. The first one occurs between 230°C and 295°C and is accompanied by a small exothermic peak at 260°C. The second one between 295°C and 315°C is accompanied by a very intense exothermic peak at 318°C, which is 20 times more intense than the one at 260°C. The mass loss and thus the composition of the compound then stabilize up to 900°C. This represents a cumulated mass loss of 25% between 230°C and 900°C, which corresponds to the complete decomposition of the cyanide bridges and their replacement by oxygen ligands. The existence of two mass losses can be explained by the presence of two kinds of Co–NC–Fe linkages in **CoFe**: the Co^{II}–NC–Fe^{III} linkages forming the as-synthesized compound and the Co^{III}–NC–Fe^{II} linkages resulting from a thermally-induced charge-transfer evidenced by infra-red spectroscopy (ESI 1†). The Co–N bond being stronger in the Co^{III}–NC–Fe^{II} linkages, we propose to assign the most exothermic transformation at higher temperature to the formation of the metal-oxygen bond formation in these particular linkages.

This TGA analysis demonstrates that 54% of the total mass is lost during the whole process: 29% because of the elimination of water molecules and 25% because of the decomposition of the cyanide bridges. If we suppose (i) that all the Co and Fe ions of the PBA precursor are part of the final phase and (ii) that the mass losses are due only to the loss of water molecules and to the replacement of the CN ligands by O ligands, the derived formula of **CoFe-Ox** is $Co_4Fe_{2.7}O_{8.9}$, which can be rewritten as $Co_{1.8}Fe_{1.2}O_4$. These results from TGA are thus fully consistent with those from EDX spectroscopy.

To summarize, the process that can be drawn from TDA/TGA is a two-steps transformation : first the elimination of water molecules and then the cyanide decomposition. This 2-step mass loss was already observed for the calcination of other PBA into oxide.[4,27,33,37] So the PBA-to-oxide transformation for the particular case of **CoFe** can be described by

$$Co_4[Fe(CN)_6]_{2.7}\bullet 19H_2O \rightarrow Co_4[Fe(CN)_6]_{2.7} \rightarrow Co_4Fe_{2.7}O_{8.9}.$$

3.4 The transformation process of CoFe

A calcination of **CoFe** during 2h in air at 900°C thus enables to get a single $Co_{1.8}Fe_{1.2}O_4$ spinel phase with a cell parameter of 8.29±0.02 Å, particle sizes ranging from 100 nm to 350 nm, an homogeneous composition of the particles and an homogeneous repartition of the transition metals inside each particle. To better understand the mechanism of this PBA-to-oxide transformation, the room temperature XRD patterns of **CoFe** after thermal treatment at variable temperatures were recorded; the most significant temperatures are displayed on Fig. 4, and the XRD patterns for all temperatures are given in ESI 2†. After the complete decomposition of the cyanide bridge of **CoFe** around 250°C (Fig. 3), a continuous evolution of the XRD patterns with temperature is observed (Fig. 4). The most striking feature is the peak splitting at 700°C, which indicates a phase separation into two phases present in approximately the same quantity (Fig. 4a,b), followed by the formation of a single phase (Fig. 4b) if the calcination is continued up to 900°C.

The XRD pattern at 300°C (Fig. 4a) displays broad peaks, that can already be indexed for a spinel structure with a unit-cell parameter of 8.22 Å. The TEM images indicate that the particle size distribution is relatively narrow and centred around 15 nm. This size is significantly smaller than the size expected for a single-particle to single-particle transformation. Therefore, the cyanide decomposition is accompanied by the fragmentation of the initial PBA particles. At 500°C (Fig. 4a), a shoulder can be seen for peaks (311), (400), (511) and (440), which suggests the beginning of a phase separation. In particular, two features can be clearly identified for peak (311) (Fig. 4a-inset) : the most intense one is centered at 36.2°2θ and the less intense shoulder at 35.5°2θ. We can therefore conclude that at 500°C, two phases with a different cell parameter exist. The phase with the lowest unit-cell parameter (i.e. at 36.2°2θ) is called *Phase 1* and the other one *Phase 2*. This phase separation continues up to 700°C, as indicated by the more pronounced splitting of the diffraction peaks; *Phase 1* remains the major phase, but its unit-cell parameter decreases.

At 700°C, all the diffraction peaks are now well separated. The comparable intensity of the peaks corresponding to the two phases expresses a similar quantity of the two phases in the sample. For *Phase 1*, the unit cell parameter of 8.19±0.02 Å is larger than for the direct spinel Co_3O_4 (8.09±0.02 Å.) but smaller than for the $CoFe_2O_4$ one (8.38±0.01 Å). This suggests that *Phase 1*

This journal is © The Royal Society of Chemistry [year]

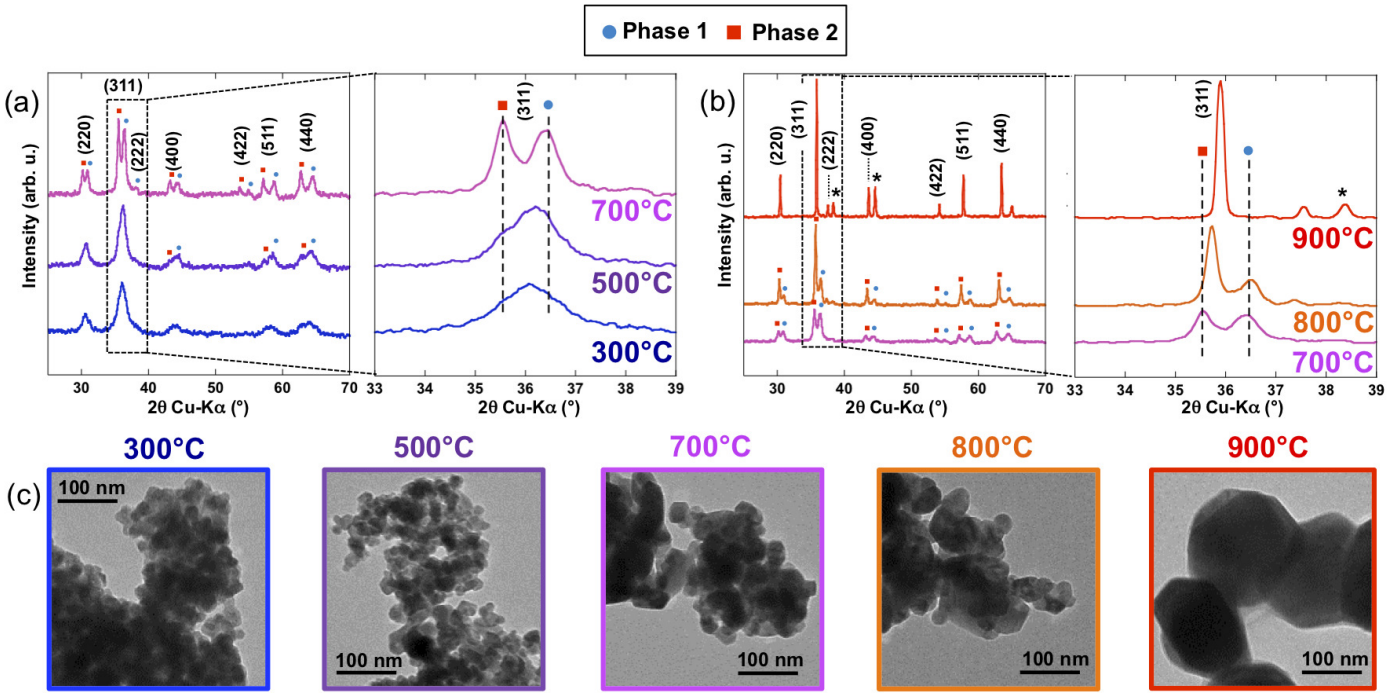

Fig. 4 X-ray diffraction patterns (a,b) and TEM images (c) of **CoFe-TT300**, **CoFe-TT500**, **CoFe-TT700**, **CoFe-TT800** and **CoFe-Ox** (900°C). A zoom of the (311) diffraction peak is presented in the inset of a and b. The diffraction peaks marked with an asterisk arise from the aluminum sample holder.

has a spinel structure, with a stoichiometry close to Co_3O_4 but with some Fe ions substituted for Co ions. In the case of *Phase 2*, the cell parameter is found to be 8.37±0.02 Å, which is the value for $CoFe_2O_4$.

Over the 300-700°C temperature range, *Phase 1* is thus the majority phase from 300°C but its lattice parameter varies. *Phase 2* already appears at 500°C, with a well-defined lattice parameter of 8.37 Å, which corresponds to the $CoFe_2O_4$ spinel, and an increasing intensity of its diffraction peaks with the increase of temperature. This evolution of the diffraction patterns over this 300-700°C range can be explained by the progressive formation of the more stable $CoFe_2O_4$ phase to the detriment of the initial spinel oxide phase. This explains the progressive shortening of its lattice parameter accompanying the increase in Co/Fe ratio in *Phase 1*. Therefore *Phase 1* acts as the reservoir for *Phase 2*, which develops if the temperature of the thermal treatment is high enough.

If the temperature is still increased up to 750°C and 800°C, an inversion of the relative intensity of the splitted peaks is observed. *Phase 2* has become the majority phase. Also, peaks appear sharper at higher temperature. The cell parameter of *Phase 1* is 8.16±0.02 Å at 750°C, which is smaller than at 700°C, and remains stable at 800°C. However, in the case of *Phase 2*, the cell parameter continuously decreases from 8.37±0.02 Å at 700°C down to 8.36±0.02 Å at 750°C and 8.33±0.02 Å at 800°C. At 850°C, the diffraction pattern display well-defined single peaks: *Phase 1* and *Phase 2* have merged in a single phase. A small shoulder is still visible at the feet of peak (311) but completely disappears after heating at 900°C, temperature at which the peaks are sharp and symmetric. The position of peak (311) is also stable at 35.9°2θ: the unit cell parameter of this final single phase is 8.29±0.02 Å, which is an intermediate value between those of the $CoFe_2O_4$ and Co_3O_4 phases. The grain size also increases up to 900°C, as visible on the TEM images (Fig. 4c), which shows a sintering effect with the increasing temperature.

To summarize, two key temperatures can be identified in the transformation of **CoFe** to **CoFe-Ox**: 700°C, at which the behavior of the two phases switches, and 900°C, at which the single **CoFe-Ox** phase is formed. Below 700°C, *Phase 2* is the well defined $CoFe_2O_4$ Fe-rich spinel oxide. Assuming that all the ions initially present in **CoFe** are also in **CoFe-Ox**, *Phase 2* is thus produced from ions present in *Phase 1*, which acts as an ion reservoir. Above 700 °C and as temperature increases, *Phase 1* is progressively incorporated into *Phase 2*, whose unit-cell parameter and so chemical composition now varies till the homogeneous $Co_{1.8}Fe_{1.2}O_4$ particles at 900°C. These observations can be compared to the case of the Co_2FeO_4 spinel, whose formation as a single phase was observed only for a calcination temperature of 900°C.[12,16] Ferreira and co-workers[12] used a low-temperature co-precipitation method followed by annealing at various temperatures between 300°C and 1000°C to synthesize the two Co_2FeO_4 and $CoFe_2O_4$ spinels. Their detailed structural and morphological characterization showed in the case of Co_2FeO_4 the presence of two spinel phases over the 300-800°C temperature range, one richer in Fe (a = 8.27 Å) and one richer in Co (a = 8.11 Å). Only the thermal treatment at 900°C led to the single Co_2FeO_4 phase. Ferreira and co-workers noticed that this narrow temperature range allowing the formation of Co_2FeO_4 is consistent with the phase diagram of Co-Fe-O described by Murray and Linnett, which predicts the stability of Co_2FeO_4 only around 900°C.[55] A later study by Panneer Muthuselvam and Bhowmik also observed this formation of Co_2FeO_4 only around 900°C, despite a different

synthesis approach.[16] They mechanically alloyed a mixed powder of stoichiometric amounts of Fe_2O_3 and Co_3O_4 with a subsequent annealing under different conditions (temperature, time). Their XRD patterns revealed the presence of a single spinel phase only for calcination at 900°C and 950°C. Below 900°C and at 1000°C, two spinel phases can be observed, one richer in Fe with a higher cell parameter and one richer in Co with a lower parameter. At 700°C, their Fe-rich phase has a cell parameter of 8.37 Å, which is identical to *Phase 2* in our case. Their Co-rich phase has a cell parameter of 8.13 Å, which is slightly lower than our *Phase 1* but consistent with the fact that our single phase at 900°C is richer in Fe ($Co_{1.8}Fe_{1.2}O_4$) than their Co_2FeO_4 phase. All these observations indicate that the formation of this particular Co-rich ferrite spinel is not related to the synthesis way but only to the final calcination temperature.

3.5 Towards a complete control of the oxide stoichiometry

The calcination at 900°C of **CoFe** thus leads to the formation of a single spinel phase with an identical Co:Fe ratio than in the PBA precursor. It tends to confirm that the stoichiometry of the oxide is fully controlled by the stoichiometry of the PBA precursor, as observed in the calcination of some other PBAs into oxides.[4,29,33] To strengthen this hypothesis, we prepared PBAs of controlled stoichiometry along the **CoFe**-**CoCo** solid-solution. Three intermediate PBA were prepared (**Co(Co25)Fe**, **Co(Co50)Fe** and **Co(Co75)Fe**) and calcinated at 900°C following the same protocol than for **CoFe**, leading to the three **Co(Co25)Fe-Ox**, **Co(Co50)Fe-Ox** and **Co(Co75)Fe-Ox** oxides.

The calcinated PBAs were first investigated by TEM and EDX spectroscopy, in order to determine the Co:Fe ratio. The three oxides consist in homogeneous particles, and the experimental Co:Fe ratio is given in Table 2. First, the EDX analyses showed that for a given stoichiometry, the chemical composition is the same for all the particles, as already observed for **CoFe-Ox**. Then, the average Co:Fe ratio measured by EDX for a given composition is really close to the one expected from the formula of the PBA precursor. This is an unambiguous confirmation that the stoichiometry of the oxide can be fully controlled by the PBA stoichiometry, even for intermediate compositions.

The XRD patterns were then used to determine the cell parameter of both the PBAs and the oxides; they are given in Table 2 and their variations along the **CoFe**-**CoCo** and the $Co_{1.8}Fe_{1.2}O_4$ - Co_3O_4 solid-solutions are diplayed in Fig. 5. A linear relationship between the Co content in the $[M(CN)_6]$ unit of the PBA and the cell parameter of both the PBAs and the oxides can be observed, which indicates that the changes in the PBA precursor directly impact the oxide. This is also another indication that the stoichiometry of the oxide is controlled by the one of the PBA; otherwise the linear relationship would have been lost for the oxide. It has to be noted that the unit-cell parameter of **Co(Co25)Fe**, whose formula is $Co_{2.1}Fe_{0.9}O_4$, is identical (8.24 Å) to the value found in literature for the $Co_{2.03}Fe_{0.97}O_4$ and $Co_{2.04}Fe_{0.96}O_4$ spinels.[12] Our new route for the synthesis of mixed oxides from PBAs is thus very reliable since, for particular stoichiometries that can be obtained via other routes, the final phase of oxide is identical.

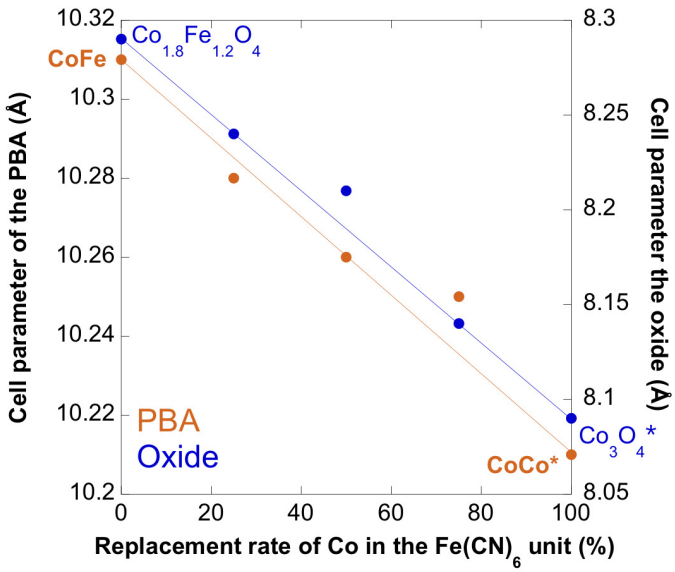

Fig. 5 Evolution of the cell parameter of the **CoFe** ($Co_4[Fe(CN)_6]_{2.7}$) - **CoCo** ($Co_4[Co(CN)_6]_{2.7}$) PBA solid-solution (orange points) and the corresponding **CoFe-Ox** ($Co_{1.8}Fe_{1.2}O_4$) - Co_3O_4 oxide solid-solution (blue points). The values for **CoCo** and Co_3O_4 (*) are taken from Ref. 35.

Fe and Co K-edges X-ray absorption spectra of the four compounds (**CoFe-Ox**, **Co(Co25)Fe-Ox**, **Co(Co50)Fe-Ox** and **Co(Co75)Fe-Ox**) are displayed in Fig. 6a and b. At both edges, the shape and energy of the spectral features are close for the four compounds, which indicates a comparable average speciation of the Co and Fe ions among the four oxides. But the most interesting feature is that the maximum of the white line at both edges linearly shifts towards higher energy when the content in Co inserted in the $[M(CN)_6]$ units increases (Fig. 6c); this linear relationship also stands if the extreme compound of the solid-solution (Co_3O_4) is included into the set of data. This clearly confirms the continuous displacement along the solid solution from **CoFe-Ox** to Co_3O_4.

The main interest in the control of the stoichiometry is the control of the property. We thus performed SQUID magnetometry measurements to investigate the magnetic property at room-temperature of the four oxides; the magnetization curve as a function of the magnetic field are displayed in Fig. 7. The magnetic properties evolve progressively along the series as an increasing amount of Co ions replaces Fe ones, in agreement with a homogeneous repartition of the Co and Fe ions within the samples without phase separation. The Co spinel oxide (Co_3O_4) is antiferromagnetic below a Néel temperature (T_N) of 35±5 K and exhibits a paramagnetic behavior above T_N.[56,57] In this compound, the octahedral and tetrahedral sites contain Co^{III}(LS) and Co^{II}(HS) ions respectively. Thus, the samples with the higher Co ions content, **Co(Co75)Fe-Ox** and **Co(Co50)Fe-Ox**, exhibit a paramagnetic behavior at 300 K like the Co spinel oxide Co_3O_4. The magnetization at 4 T, slightly higher in **Co(Co50)Fe-Ox** (0.15 μ_B) than in Co(Co75) (0.05 μ_B) can be explained by an increasing replacement of the Co^{III}(LS) (S = 0) and/or Co^{II}(HS) (S = 3/2) ions by Fe^{III}(HS) (S = 5/2) and/or Fe^{II}(HS) (S = 2) ones. As

This journal is © The Royal Society of Chemistry [year]

Table 2 Cell parameter and formula of the PBA and oxides along the **CoFe**-Co_3O_4 solid-solution. The value for the end member are reminded.

Replacement rate of Co in the $Fe(CN)_6$ unit	PBA Formula	PBA Unit cell parameter	Oxide Formula	Oxide Unit cell parameter	Co:Fe ratio from EDX	Co:Fe ratio Expected
0 %	$Co_4[(Fe(CN)_6]_{2.7}$	10.31 Å	$Co_{1.8}Fe_{1.2}O_4$	8.29 Å	1.4	1.5
25 %	$Co_4[(Fe_{0.75}Co_{0.25})(CN)_6]_{2.7}$	10.28 Å	$Co_{2.1}Fe_{0.9}O_4$	8.24 Å	2.1	2.3
50 %	$Co_4[(Fe_{0.50}Co_{0.50})(CN)_6]_{2.7}$	10.26 Å	$Co_{2.4}Fe_{0.6}O_4$	8.21 Å	3.7	4.0
75 %	$Co_4[(Fe_{0.25}Co_{0.75})(CN)_6]_{2.7}$	10.24 Å	$Co_{2.7}Fe_{0.3}O_4$	8.14 Å	8.0	9.0
100 %	$Co_4[Co(CN)_6]_{2.7}$	10.21 Å	Co_3O_4	8.09 Å	/	/

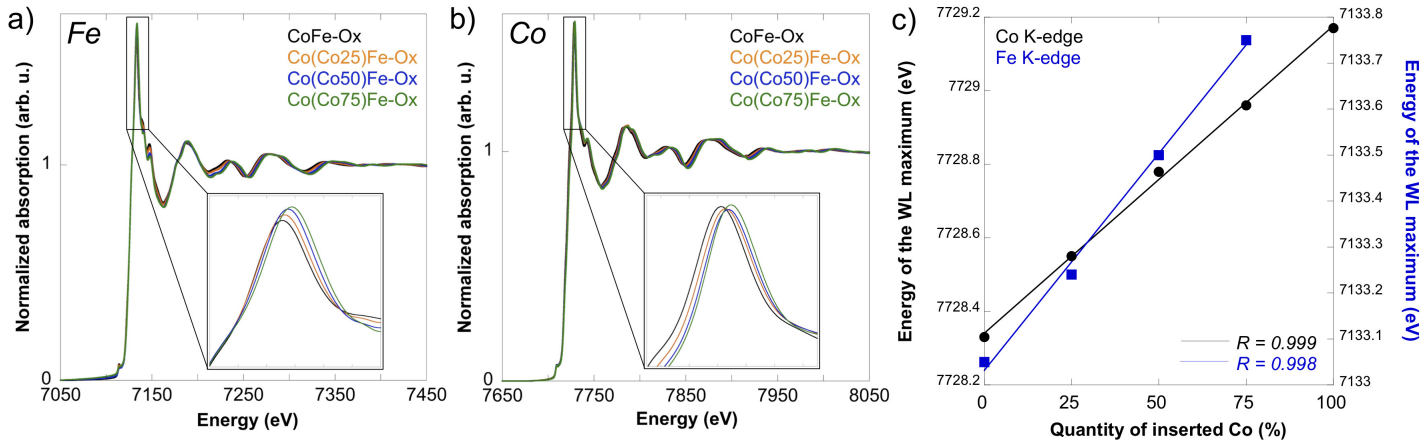

Fig. 6 (a) Fe and (b) Co K-edges X-ray absorption spectra of **CoFe-Ox**, **Co(Co25)Fe-Ox**, **Co(Co50)Fe-Ox** and **Co(Co75)Fe-Ox**, with a zoom on the maximum of the white line. (c) Evolution of the energy of the white line maximum in the oxides along the **CoFe**-Co_3O_4 solid-solution; the dots represent the experimental values and the line the corresponding linear regression.

the amount of Fe ions still increases, an hysteresis loop appears revealing a room-temperature magnet behavior for **Co(Co25)Fe-Ox** and **CoFe-Ox**. The increase in saturation magnetization and in coercive field from one compound to the other can again be explained by the progressive replacement of Co ions by Fe ones.

To summarize, all these results on the calcination of **CoFe** into **CoFe-Ox** and on the three intermediate compositions along the **CoFe**-Co_3O_4 solid-solution clearly demonstrate that the stoichiometry of the PBA precursor fully controls the stoichiometry of the mixed oxide.

3.6 Transposition of the process at the nanoscale

The results presented in the previous sections demonstrate the successful transformation of the PBA into a mixed oxide with controlled stoichiometry. However, one of the main interest of a functional material for application is the possibility to shape it at a nanoscale, as shown by the several investigations on the synthesis process and properties of ferrite nanoparticles.[3,5,18,58–63] Therefore we tried to transpose the transformation of **CoFe** into **CoFe-Ox** at the nanoscale by combining the formation of a mixed oxide from a PBA (this work) and the control growth of PBA nanoparticles inside the porosity of a mesoporous silica monolith. Some of our previous works indeed demonstrated that the confinement of **CoFe** growth inside the pores of a mesoporous silica monolith[35,40,44–48] leads to the formation of nanoparticles whose size is controlled by the size of the pores. We first tested this combined

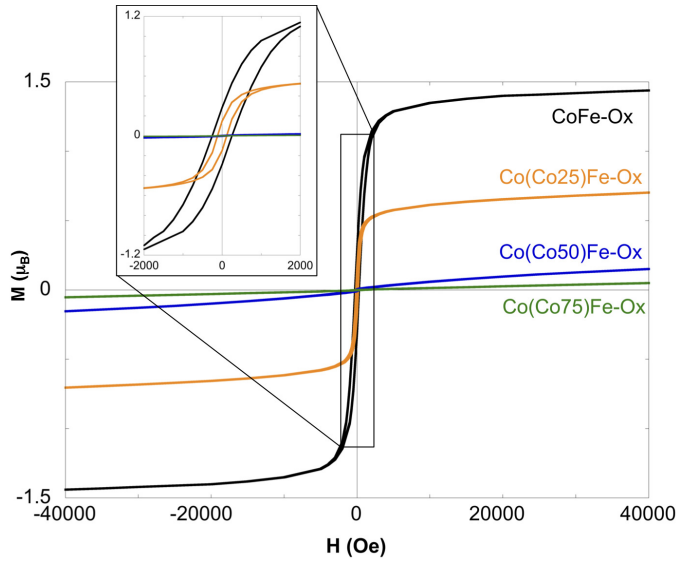

Fig. 7 Evolution of the magnetization as a function of the magnetic field at room temperature for the 4 oxides **CoFe-Ox**, **Co(Co25)Fe-Ox**, **Co(Co50)Fe-Ox** and **Co(Co75)Fe-Ox**.

approach with the simple case of the calcination of monometallic PBA nanoparticles; we obtained oxide nanoparticles of controlled and monodispersed size, with the expected Co_3O_4 spinel structure and composition.[35] Here we confined **CoFe** into the 4.5 nm-pores of a mesoporous silica (this new precursor is called **NanoCoFe**) and then applied the thermal treatment to **NanoCoFe**, in order to get 5 nm-particles of the $Co_{1.8}Fe_{1.2}O_4$ mixed oxide (called **NanoCoFe-Ox**, as the particles remain in the porosity).

The thermodifferential and thermogravimetric analyses are shown in Fig. 8a. As for **CoFe**, two mass losses are observed. The first one occurs until 115°C and corresponds to the elimination of water from both the silica and the PBA structure; 11% of the total mass is thus lost. Then, a mass loss of 4% spreads until 310°C; it is accompanied by a unique exothermic peak at 282°C, which corresponds to the cyanide bridge decomposition. Above 310°C, the mass loss slightly continues because of the silica matrix condensation under heating.

The chosen temperature for the thermal treatment of **NanoCoFe** (700°C) is a compromise between the temperature required to transform the **CoFe** into **CoFe-Ox** and the one that keeps intact the ordered mesoporous structure of the silica. The TEM image of longitudinal section of **NanoCoFe-Ox** (Fig. 8b) nicely shows the preservation of the silica organization after the thermal treatment, as previously observed for the transformation of a Co monometallic PBA into Co_3O_4.[35] Almost all parallel pores of the silica contain spherical particles. The HR-TEM image of one of these particles (Fig. 8c) shows the parallel lines corresponding to reticular planes of a single-crystalline particle. The average measured distance between two successive lattice planes (0.242± 0.004 nm) of this single-crystal corresponds to an interplanar distance consistent with the (311) *d*-spacing of a CoFe spinel oxide. EDX spectroscopy could be performed on the particles (Fig. 8d), and the Co:Fe ratio is found to be 1.5, as expected from the Co:Fe ratio in **NanoCoFe** particles and also the **CoFe-Ox** ones (Fig. 2b). Finally, a statistical analysis of the particle size reveals that the average size is 4.5 nm with a narrow size distribution (Fig. 8e); it means that the particles fill the entire diameter of the pores, indicating that the particles size is controlled by the pore size.

Therefore, **NanoCoFe-Ox** can be described as an ordered mesoporous silica monolith containing single-crystalline CoFe spinel nanoparticles within its porosity. Given the Co:Fe ratio of 1.5 as for **CoFe-Ox**, the deduced stoichiometry of the nanoparticles is $Co_{1.8}Fe_{1.2}O_4$. The confinement of the PBA particles may thus influence the calcination process, as suggested by the lower calcination temperature for **NanoCoFe** with respect to **CoFe**, but it does not prevent the formation of homogeneous single-crystalline nanoparticles. This synthesis route for oxide nanoparticles is compared to the more conventional mixing of nitrate salts in our reference 64, along a detailed investigation of the magnetic properties of the nanoparticles. A detailed investigation of the impact of confinement and of the synthesis conditions of the confined PBA on the calcination process will be presented in an upcoming publication.

4 Conclusion

We presented here the successful synthesis of mixed Co-Fe oxides with a fine control of their stoichiometry through the controlled variation of the Co:Fe ratio in their PBA precursor. The thermal treatment, derived from our previous investigations of the transformation of a Co monometallic PBA into Co_3O_4,[35,54] was optimized thanks to a detailed XRD investigation of the calcination process. In the case of **CoFe**, we demonstrate here that a single-crystalline single phase can be obtained only around 900°C with a 2-phases intermediate step, as observed for the synthesis of $FeCo_2O_4$ by other techniques.[12,16] The characterization of these intermediate spinel phases and of the kinetics effects is in progress and will bring a deep insight into the calcination mechanism; in particular, in situ Co and Fe K-edges X-ray absorption spectroscopy experiments were recently performed to characterize at the local scale the variation of the Fe and Co electronic structure and local environment during the calcination process. Also, the versatility of this synthesis route is successfully demonstrated with our present results for mixed oxides and nanoparticles. It has to be noted that we and other groups also successfully extend the use of PBA as precursors to (i) the case of alloys[34,64–67] and (ii) the formation of nanoparticles in other matrices templates such as perforated thin films.[68,69]

To conclude, our results, combined with literature, definitively confirm that PBA are the most versatile, controllable and reliable precursors for the synthesis of oxides with a controlled stoichiometry and particle size. This offers a unique way to design oxides with targeted properties.

Conflicts of interest

There are no conflict of interest to declare.

Acknowledgments

V. Trannoy thanks the Région Ile-de-France C'Nano program (no. GDR2972) for the PhD financial support. MIR spectroscopy analyses were obtained by Kevin Privat during its internship. The XAS experiments on the ROCK beamline were supported by a public grant overseen by the French National Research agency (ANR) as part of the "Investissements d'Avenir" program (reference ANR-10-EQPX-45). The authors acknowledge SOLEIL for the provision of synchrotron radiation facilities through proposal 20160306.

Notes and references

1 E. Casbeer, V. K. Sharma and X.-Z. Li, *Separation and Purification Technology*, 2012, **87**, 1–14.
2 S. Jauhar, J. Kaur, A. Goyal and S. Singhal, *RSC Advances*, 2016, **6**, 97694–97719.
3 K. K. Kefeni, T. A. Msagati and B. B. Mamba, *Materials Science and Engineering B*, 2017, **215**, 37–55.
4 L. Hu, Y. Huang and Q. Chen, *Journal of Alloys and Compounds*, 2013, **559**, 57–63.
5 X. Li, Z. Wang, B. Zhang, A. I. Rykov, M. A. Ahmed and J. Wang, *Applied Catalysis B: Environmental*, 2016, **181**, 788–799.

This journal is © The Royal Society of Chemistry [year]

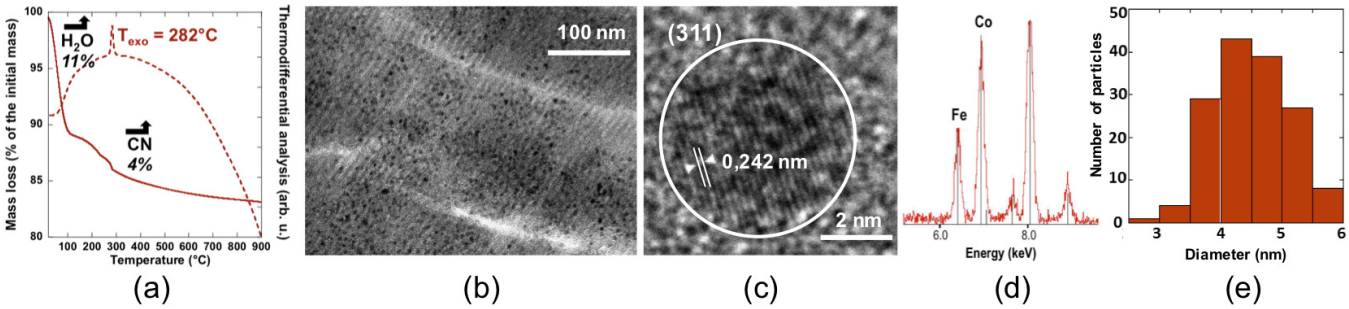

Fig. 8 (a) TDA/TGA pattern recorded for **NanoCoFe** with a heating rate of 5°C.min^{-1} in air (the continuous line is the mass and the dashed line the thermodifferential analysis). (b) TEM image of a longitudinal section (prepared by microtomy) of **NanoCoFe-Ox**, (c) HR-TEM image and the (d) corresponding EDX spectrum of a particle, and (e) histogram of the particle size distribution.

6 M. Lv, X. Guo, Z. Wang, L. Wang, Q. Li and Z. Zhang, *RSC Advances*, 2016, **6**, 27052–27059.

7 D. H. K. Reddy and Y.-S. Yun, *Coordination Chemistry Review*, 2016, **35**, 90–111.

8 A. Šutka and K. A. Gross, *Sensors and Actuators B: Chemical*, 2016, **222**, 95–105.

9 D. H. Taffa, R. Dillert, A. C. Ulpe, K. C. L. Bauerfeind, T. Bredow, D. W. Bahnemann and M. Wark, *Sensors and Actuators B: Chemical*, 2016, **222**, 95–105.

10 J. Zhang, L. Wang, L. Xu, X. Ge, X. Zhao, M. Lai, Z. Liu and W. Chen, *Nanoscale*, 2015, **7**, 720–726.

11 F. Zhao, J. Tian and B. Wang, *Materials Letters*, 2015, **161**, 104–107.

12 T. Ferreira, J. Waerenborgh, M. Mendonca, M. Nunes and F. Costa, *Solid State Sciences*, 2003, **5**, 383–392.

13 Y. Qi, Y. Yang, X. Zhao, X. Liu, P. Wu, F. Zhang and S. Xu, *Materials Letters*, 2006, **60**, 3548–3552.

14 P. Aghav, V. N. Dhage, M. L. Mane, D. Shengule, R. Dorik and K. Jadhav, *Physica B*, 2011, **406**, 4350–4354.

15 A. M. Wahba and M. B. Mohamed, *Journal of Magnetism and Magnetic Materials*, 2015, **378**, 246–252.

16 I. Panneer Muthuselvam and R. N. Bhowmik, *Solid State Sciences*, 2009, **11**, 719–725.

17 A. P. Herrera, L. Polo-Corrales, E. Chavez, J. Cabarcas-Bolivar, O. N. Uwakweh and C. Rinaldi, *Journal of Magnetism and Magnetic Materials*, 2013, **328**, 41–52.

18 M. Houshiar, F. Zebhi, Z. J. Razi, A. Alidoust and Z. Askari, *Journal of Magnetism and Magnetic Materials*, 2014, **371**, 43–48.

19 M. G. Naseri, E. B. Saion, H. A. Ahangar, A. H. Shaari and M. Hashim, *Journal of Nanomaterials*, 2010, **2010**, 907686.

20 Y. Qu, H. Yang, N. Yang, Y. Fan, H. Zhu and Z. Guangtian, *Particuology*, 2010, **8**, 207–211.

21 M. Shi, R. Zuo, Y. Xu, Y. Jiang, G. Yu, H. Su and J. Zhong, *Journal of Alloys and Compounds*, 2012, **512**, 165–170.

22 V. Sudheesh, N. Thomas and P. a. S. V. Roona, N. ans Baghya, *Ceramics International*, 2017, **43**, 15002–15009.

23 P. R. Varma, R. S. Manna, B. D., M. R. Varma, K. Suresh and A. Nigam, *Journal of Alloys and Compounds*, 2008, **453**, 298–303.

24 J. Wang, T. Deng, Y. Lin, C. Yang and W. Zhan, *Journal of Alloys and Compounds*, 2008, **450**, 532–539.

25 L. Han, X.-Y. Yu and X. W. D. Lou, *Advanced Materials*, 2016, **28**, 4601–4605.

26 X. Hou, G. Zhu, X. Niu, Z. Dai, Z. Yin, Q. Dong, Y. Zhang and X. Dong, *Journal of Alloys and Compounds*, 2017, **729**, 518–525.

27 X. Li, L. Yuan, J. Wang, L. Jiang, A. I. Rykov, D. L. Nagy, C. Bogdán, M. A. Ahmed, G. Zhu, Kaiyue adnd Sun and W. Yang, *Nanoscale*, 2016, **8**, 2333–2342.

28 S. Rohilla, B. Lal, S. Sunder, P. Aghamkar, S. Kumar and A. Aggarwal, *Acta Physica Polonica A*, 2010, **118**, 696–700.

29 M. B. Zakaria, M. Hu, M. Imura, R. R. Salunkhe, N. Umezawa, H. Hamoudi, A. A. Belik and Y. Yamauchi, *Chemistry - A European Journal*, 2014, **20**, 17375–17384.

30 M. B. Zakaria, M. Hu, N. Hayashi, Y. Tsujimoto, S. Ishihara, M. Imura, N. Suzuki, Y.-Y. Huang, Y. Sakka, K. Ariga, K. C.-W. Wu and Y. Yamauchi, *European Journal of Inorganic Chemistry*, 2014, **2014**, 1137–1141.

31 M. B. Zakaria, M. Hu, M. Pramanik, C. Li, J. Tang, A. Aldalbahi, S. M. Alshehri, V. Malgraas and Y. Yamauchi, *Chemistry - An Asian Journal*, 2015, **10**, 1541–1545.

32 M. B. Zakaria, M. S. A. Hossain, M. J. A. Shiddiky, M. Shahabuddin, E. Yanmaz, J. H. Kim, A. A. Belik, Y. Ide, M. Hu, S. Tominaka and Y. Yamauchi, *Chemistry - A European Journal*, 2016, **22**, 15042–15048.

33 M. B. Zakaria, C. Li, M. Pramanik, Y. Tsujimoto, M. Hu, V. Malgras, S. Tominaka and Y. Yamauchi, *Journal of Materials Chemistry A*, 2016, **4**, 9266–9274.

34 M. B. Zakaria and T. Chikyow, *Coordination Chemistry Review*, 2017, **352**, 328–345.

35 V. Trannoy, E. Delahaye, G. Fornasieri, P. Beaunier and A. Bleuzen, *Comptes Rendus Chimie*, 2014, **17**, 512–520.

36 R. Zboril, L. Machala, M. Mashlan and V. Sharma, *Crystla Growth and Design*, 2004, **4**, 1317–1325.

37 L. Zhang, L. Shi, J. Huang, R. Gao and D. Zhang, *ACS Catalysis*, 2014, **4**, 1753–1763.

38 X. Zhao, F. Li, B. Li, T. Zhang, Q. Teng, L. Wang, H. Wang and Y. Zhang, *Journal of Physics and Chemistry of Solids*, 2018,

113, 134–141.
39 V. Escax, *PhD thesis*, Université Paris VI, 2002.
40 G. Fornasieri, M. Aouadi, P. Durand, E. Rivière and A. Bleuzen, *Chem. Comm.*, 2010, **46**, 8061–8063.
41 M. Imperor-Clerc, D. Bazin, M.-D. Appay, P. Beaunier and A. Davidson, *Chemistry of Materials*, 2004, **16**, 1813–1821.
42 I. Lopes, N. El Hassan, H. Guerba, G. Wallez and A. Davidson, *Chemistry of Materials*, 2006, **18**, 5826–5828.
43 J. Van der Meer, I. Bardez-Giboire, C. Mercier, B. Revel, A. Davidson and R. Denoyel, *Journal of Physical Chemistry C*, 2010, **114**, 3507–3515.
44 P. Durand, G. Fornasieri, C. Baumier, P. Beaunier, D. Durand, E. Rivière and A. Bleuzen, *Journal of Materials Chemistry*, 2010, **20**, 9348–9354.
45 E. Delahaye, R. Moulin, M. Aouadi, V. Trannoy, P. Beaunier, G. Fornasieri and A. Bleuzen, *Chemistry - A European Journal*, 2015, **21**, 16906–16916.
46 R. Moulin, E. Delahaye, A. Bordage, E. Fonda, J.-P. Baltaze, P. Beaunier, E. Rivière, G. Fornasieri and A. Bleuzen, *European Journal of Inorganic Chemistry*, 2017, **2017**, 1303–1313.
47 G. Fornasieri, A. Bordage and A. Bleuzen, *European Journal of Inorganic Chemistry*, 2018, **2018**, 259–271.
48 M. Aouadi, G. Fornasieri, V. Briois, P. Durand and A. Bleuzen, *Chemistry - A European Journal*, 2012, **18**, 2617–2623.
49 V. Trannoy, *PhD thesis*, Université Paris-Saclay, 2015.
50 V. Briois, C. La Fontaine, S. Belin, L. Barthe, T. Moreno, V. Pinty, A. Carcy, R. Girardot and E. Fonda, *Journal of Physics: Conference Series*, 2016, **712**, 012149.
51 A. Bleuzen, C. Lomenech, V. Escax, F. Villain, F. Varret, C. Cartier dit Moulin and M. Verdaguer, *Journal of the American Chemical Society*, 2000, **122**, 6648–6652.
52 A. Bleuzen, J.-D. Cafun, A. Bachschmidt, M. Verdaguer, P. Münsch, F. Baudelet and J.-P. Itié, *Journal of Physical Chemistry C*, 2008, **112**, 17709–17715.
53 X. Liu and C. T. Prewitt, *Physical and Chemistry of Minerals*, 1990, **17**, 168–172.
54 A. Bordage, V. Trannoy, O. Proux, H. Vitoux, R. Moulin and A. Bleuzen, *Physical Chemistry Chemical Physics*, 2015, **17**, 17260–17265.
55 P. J. Murray and J. W. Linnett, *Journal of Physics and Chemistry of SOlids*, 1976, **37**, 619–624.
56 P. Dutta, M. Seerha, S. Thota and J. Kumar, *Journal of Physics: Condensed Matter*, 2008, **20**, 015218.
57 G. Wang, X. Shen, J. Horvat, B. Wang, H. Liu, D. Wexler and J. Yao, *The Journal of Physical Chemsitry C*, 2009, **113**, 4357–4361.
58 Y. I. Kim, D. Kim and C. S. Lee, *Physica B*, 2003, **337**, 42–51.
59 X. Li and C. Kutal, *Journal of Alloys and Compounds*, 2003, **349**, 264–268.
60 L. Garcìa-Cerda, V. Torres-Garcìa, J. Matutes-Aquino and O. Ayala, Valenzuela, *Journal of Alloys and Compounds*, 2004, **369**, 148–151.
61 D. Carta, M. Casula, A. Falqui, D. Loche, G. Mountjoy, C. Sangregorio and A. Corrias, *Journal of Physical Chemistry C*, 2009, **113**, 8606–8615.
62 S. Nappini, E. Magnano, F. Bondino, I. Pis, A. Barla, E. Fantechi, F. Pineider, C. Sangregoria, L. Vaccari, L. Venturelli and P. Baglioni, *The Journal of Physical Chemistry C*, 2015, **119**, 25529–25541.
63 U. Wrongpratat, S. Maensiri and E. Swatsitang, *Microelectronic Engineering*, 2015, **146**, 68–75.
64 V. Trannoy, L. Altenschmidt, G. Fornasieri, A. Bordage, E. Rivière, P. Beaunier and A. Bleuzen, *ChemNanoMat*, 2018, **4**, 1254–1261.
65 C. Aparicio, L. Machala and Z. Marusak, *Journal of Thermal Analysis and Calorimetry*, 2012, **110**, 661–669.
66 C. W. Ng, J. Ding, L. Wang, L. M. Gan and C. Quek, *Journal of Physical Chemistry A*, 2000, **104**, 8814–8822.
67 C. W. Ng, J. Ding, Y. Shi and L. M. Gan, *Journal of Physics and Chemsitry of Solids*, 2001, **62**, 767–775.
68 V. Trannoy, M. Faustini, D. Grosso, S. Mazerat, F. Brisset, A. Dazzi and A. Bleuzen, *Beilstein Journal of Nanotechnology*, 2014, **15**, 1933–1943.
69 V. Trannoy, M. Faustini, D. Grosso, F. Brisset, P. Beaunier, E. Rivière, M. Putero and A. Bleuzen, *Nanoscale*, 2017, **9**, 5234–5243.

This journal is © The Royal Society of Chemistry [year]

Towards the synthesis of mixed oxides with controlled stoichiometry from Prussian Blue analogues

Virgile Trannoy,[a‡] Amélie Bordage,*[a] Jordan Dezalay,[a] Romuald Saint Martin,[a] Eric Rivière,[a] Patricia Beaunier,[b] Cédric Baumier,[c] Camille La Fontaine,[d] Giulia Fornasieri,[a] and Anne Bleuzen[a]

[a] ICMMO, Université Paris-Sud, Université Paris-Saclay, CNRS, Rue du doyen Georges Poitou, 91405 Orsay Cedex, France. Tel: +33 1 69 15 32 07; E-mail: anne.bleuzen@u-psud.fr
[b] Sorbonne Université, CNRS, Laboratoire de Réactivité de Surface, LRS, F-75005 Paris, France
[c] Centre des Sciences Nucléaires et de la Matière, Université Paris-Sud, CNRS/IN2P3, Université Paris-Saclay, 91405 Orsay Cedex, France
d Synchrotron SOLEIL, Saint Aubin, 91190 Gif-sur-Yvette, France
[‡] Present address : ILV, Université Versailles Saint-Quentin en Yvelines, UMR CNRS 8180, 45 avenue des Etats-Unis, 78035 Versailles Cedex, France

SUPPLEMENTARY INFORMATION

ESI 1 — Evidence by Infra-Red spectroscopy of a thermally-induced charge transfer in CoFe below 300°C

Middle infra-red spectroscopy measurements were performed on the precursor PBA (**CoFe**) and on the calcinated samples. We used a VERTEX70 spectrometer (Brüker) in the reflexion mode, with a resolution of 4 cm^{-1}.

The spectra of **CoFe** in the early stages of calcination are displayed in figure S1; the assignment of the IR spectral features is done according to literature [s1-s4]. The first band centred at 2157 cm^{-1} is the signature of a Co^{II}—NC—Fe^{III} linkage in a PBA. While heating up to 200°C, the intensity of this band is decreasing, while two bands appear around 2120 cm^{-1} and 2090 cm^{-1}; they are respectively characteristic of the Co^{III}—NC—Fe^{II} and Co^{II}—NC—Fe^{II} linkages in a PBA. This indicates that prior the decomposition of the cyanide bridge around 300°C, a thermally induced charge transfer from Co^{II}—NC—Fe^{III} towards Co^{III}—NC—Fe^{II} occurs. The presence of these two linkages explain the two mass losses observed by TDA/TGA between 240°C and 330°C, which correspond to the decomposition of each kind of Co—NC—Fe linkages in the PBA.

Also, as (i) all IR bands in the cyanide stretching vibration range can definitely be assigned to cyanide in Co-NC-Fe environments with different oxidation states of the transition metal ions and (ii) no band corresponding to CO vibration appears on the spectrum, the presence of cyanate can be ruled out.

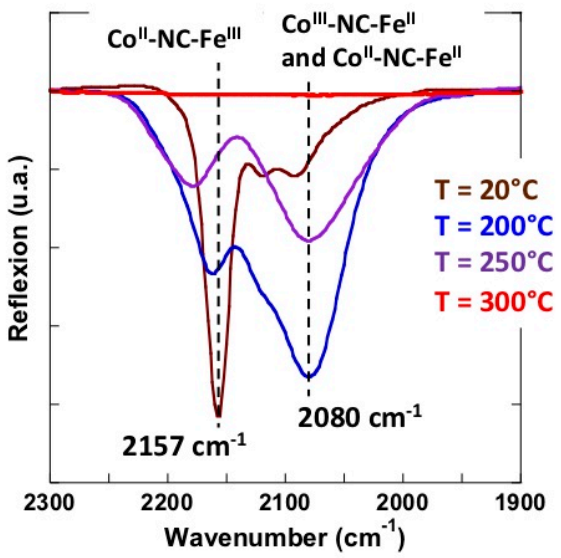

Figure S1. Infrared spectra on the cyanide bridge vibration range of **CoFe** before (20°C) and during early calcination before the cyanide bridge decomposition (200°C, 250°C and 300°C).

[s1] O. Sato, Y. Einaga, A. Fujishima and K. Hashimoto, *Inorganic Chemistry*, 1999, **38**, 4405-4412. (and references within)

[s2] R.O. Lezna, R. Romagnoli, N.R. de Tacconi and K. Rajeshwar, *Journal of Physical Chemistry B*, 2002, **106**, 3612-3621. (and references within)

[s3] N. Shimamoto, S-I. Ohkoshi, O. Sato and K. Hashimoto, I*norganic Chemistry*, 2002, **41**, 678-684.

[s4] J. Lejeune, J-B. Brubach, P. Roy and A. Bleuzen, *Comptes Rendus Chimie*, 2014, **17**, 534-540.

ESI 2 — Complete set of X-ray diffraction patterns between 300°C and 900°C

The **CoFe-TTXXX** samples (TT = Thermal Treatment; XXX= calcination temperature) were obtained after the calcination of **CoFe** at different temperatures in order to investigate in details the calcination process. The whole set of XRD patterns are displayed in Figure S2.
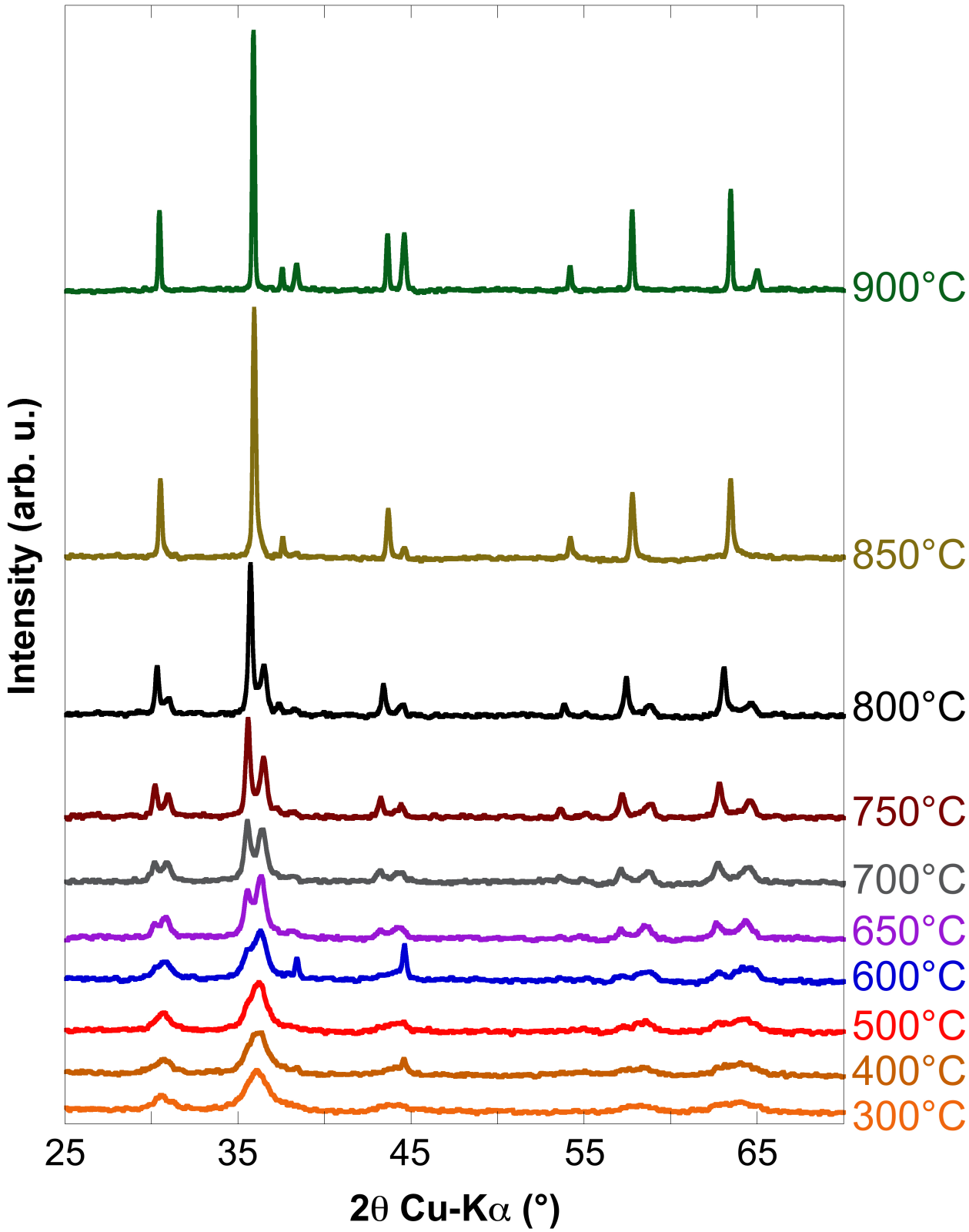
Figure S2. XRD patterns of the **CoFe-TTXXX** samples between 300°C and 900°C